



Cite this: *Nanoscale Adv.*, 2021, **3**, 3563

Morphology-dependent fluorescence of europium-doped cerium oxide nanomaterials[†]

Anne E. D'Achille,^a Robert M. Wallace^b and Jeffery L. Coffer^{a*}

Europium-doped CeO_2 nanomaterials have been investigated for a variety of sensing and biological applications, as doping enhances the catalytic activity of CeO_2 and contributes visible fluorescence to the nanomaterial. However, scant evidence is available that directly compares Eu^{3+} fluorescence from multiple morphologies establishing useful correlation(s) between physical and optical trends in such structures. To address this shortcoming, Eu^{3+} -doped CeO_2 nanorods, nanowires, nanocubes, and annealed nanorods were synthesized and characterized, representing a range of crystalline defect sizes, defect concentrations, and surface moieties. Morphologies rich with oxygen defects and hydroxyl groups (assessed via X-ray photoelectron spectroscopy) quenched the Eu^{3+} fluorescence, while samples with larger crystalline domains and lower Ce^{3+} concentrations have relatively stronger emission intensities. Of the four morphologies, nanocubes exhibit the strongest emission, as each structure is monocrystalline with few oxygen defects and associated quenching sites. Furthermore, the Eu^{3+} hypersensitive transition is more responsive to the dopant concentration in the nanocubes, as defects induced by the dopant are not removed by thermal annealing.

Received 5th February 2021
Accepted 27th April 2021

DOI: 10.1039/d1na00096a
rsc.li/nanoscale-advances

Introduction

Interest in cerium oxide (CeO_2) nanomaterials continues to grow at a significant pace, due to ever-expanding applications in three-way catalytic converters,¹ solid oxide fuel cells,^{2,3} radio-protective agents,⁴ oxygen⁵ and biological sensors,⁶ and enzyme mimetics,^{7,8} among others. This versatility stems from cerium's ability to easily convert between Ce^{3+} and Ce^{4+} oxidation states, as facilitated by the adsorption or release of oxygen. Methods to synthesize CeO_2 nanomaterials have been extensively explored, with popular approaches including controlled precipitation,^{9,10} hydrothermal,^{11–13} sol-gel,^{14,15} surfactant-assisted,¹⁶ electrodeposition,¹⁷ and micellar methods. A range of morphologies including rods,^{11,12} cubes,¹⁸ wires,¹⁹ tubes,²⁰ and polyhedral¹³ particles have been synthesized by adjusting the reaction parameters.

Cerium is predominantly present as Ce^{4+} within the CeO_2 structure, with a small concentration of Ce^{3+} defects charge balanced by oxygen vacancies.²¹ Manipulation of the ratio of Ce^{3+} to Ce^{4+} within a nanomaterial controls the nature of the CeO_2 chemical activity as seen with the material's enzyme mimetic activity.^{8,22,23} Ce^{3+} -rich materials act as superoxide dismutase mimetics, while Ce^{4+} -rich samples mimic

catalase.^{7,8,24} Reducing the nanoparticle dimensions^{25,26} and doping with lower-valent ions^{27,28} are two common approaches to increase the $\text{Ce}^{3+}/\text{Ce}^{4+}$ ratio, which is accompanied by an increase in oxygen vacancy concentration to maintain balanced charge within the nanomaterial.^{25–29}

Other rare earth ions, which prefer the +3 oxidation state in many oxide phases, are easily doped into CeO_2 nanomaterials due to similar ionic radii. The lower oxidation state of the dopant generates oxygen vacancies as well as Ce^{3+} defects to maintain charge balance.^{26,28} The resulting Ln^{3+} -doped CeO_2 ($\text{Ln}-\text{CeO}_2$) nanomaterials have altered oxygen mobility, magnetism, catalytic reactivity, and fluorescence compared to the CeO_2 host.^{30–32} In addition to controlling the $\text{Ce}^{3+}/\text{Ce}^{4+}$ ratio, doping CeO_2 nanomaterials with known lanthanide fluorophores makes the structure fluorescent, eliminating the need for surface functionalization using fluorescent labels *via* post-fabrication processing.^{33–38}

In terms of lanthanide ion choices, europium(III) is known for its intense red-orange emission and hypersensitive $^5\text{D}_0 \rightarrow ^7\text{F}_2$ transition. This transition is permitted only in the absence of an inversion symmetry, so the fluorescence associated with this hypersensitive transition in Eu^{3+} has been used in metal complexes and metal-organic frameworks as sensors/biosensors.^{39–43} The factors controlling fluorescence from the $\text{Eu}-\text{CeO}_2$ nanoparticle morphology are the most thoroughly studied,^{44,45} with less thorough investigation of $\text{Eu}-\text{CeO}_2$ films, rods, and nanowires or ribbons.^{33,34,38,46–48} Emission is believed to initiate with excitation of the $\text{O}^{2-} \rightarrow \text{Ce}^{4+}$ charge transfer band, followed by energy transfer to Eu^{3+} and relaxation with emission of

^aDepartment of Chemistry and Biochemistry, Texas Christian University, Ft. Worth, TX, 76129, USA. E-mail: j.coffer@tcu.edu

^bDepartment of Materials Science and Engineering, University of Texas at Dallas, Dallas, TX 75080, USA

† Electronic supplementary information (ESI) available. See DOI: [10.1039/d1na00096a](https://doi.org/10.1039/d1na00096a)



a photon. Ce^{3+} defects are proposed to aid the emission from Eu^{3+} , but are typically accompanied by other intrinsic defects (oxygen vacancies, OH^- groups, *etc.*) that facilitate non-radiative relaxation.^{33,49} Annealing removes these defects and associated non-radiative pathways, increasing overall emission intensity but weakens the hypersensitive transition in the 610–630 nm range as the removal of defects increases the symmetry about the Eu^{3+} .⁴⁶

At low dopant concentrations, emission intensity from $\text{Eu}-\text{CeO}_2$ nanomaterials typically strengthens as the Eu^{3+} concentration is increased.^{34,47} Elevated dopant concentrations are associated with a stronger contribution from the hypersensitive transition, due to the introduction of defects.^{38,47,50} As the dopant concentration increases, the internal defects become more concentrated and the distance between Eu^{3+} ions is diminished, increasing the likelihood of self-quenching. Above a morphologically-dependent limit, quenching from these defects or other lanthanide ions prevents Eu^{3+} emission from the $\text{Eu}-\text{CeO}_2$ nanomaterial.^{51,52}

While considerable research is available regarding the photophysical properties of various $\text{Eu}-\text{CeO}_2$ morphologies, many of these studies are focus only on one morphology or one dopant concentration, so a systematic comparison of emission as a function of morphology is lacking. In this paper, we report the synthesis and thorough characterization (scanning and transmission electron microscopies, energy dispersive X-ray spectroscopy, X-ray diffraction) of a well-defined series of morphologies through hydrothermal and electrospinning/annealing techniques. By comparing the optical properties of samples with similar dopant concentrations, we demonstrate the significant morphological dependence of emission intensity and asymmetry, associated with differences in surface chemistry, oxygen vacancy concentrations and $\text{Ce}^{3+}/\text{Ce}^{4+}$ ratios (as monitored indirectly by X-ray Photoelectron Spectroscopy (XPS)), and crystalline domain dimensions. Furthermore, the impact of Eu^{3+} concentration on the overall emission intensity, especially the hypersensitive transition, is found to be highly sensitive to CeO_2 host morphology.

Methods and materials

All reagents purchased were of analytical grade. Polyvinylpyrrolidone (PVP, $M_w \sim 1\,300\,000$), dimethyl-formamide (DMF), and methanol (MeOH) were purchased from Sigma Aldrich. MeOH and DMF were stored with molecular sieves. PVP was heated to 95 °C for 6 h, vacuum dried at room temperature overnight, and stored in a desiccator. All other chemicals were used as received with no further purification. Acetone and ethanol (95%) were purchased from Pharmco-Aaper. Cerium(III) chloride heptahydrate ($\text{CeCl}_3 \cdot 7\text{H}_2\text{O}$), europium(III) nitrate hexahydrate ($\text{Eu}(\text{NO}_3)_3 \cdot 6\text{H}_2\text{O}$), and sodium hydroxide (NaOH) were purchased from Alfa Aesar. Europium(III) chloride hexahydrate ($\text{EuCl}_3 \cdot 6\text{H}_2\text{O}$) was purchased from Strem. Cerium(III) nitrate heptahydrate ($\text{Ce}(\text{NO}_3)_3 \cdot 7\text{H}_2\text{O}$) was purchased from Acros Organics. Tribasic sodium phosphate dodecahydrate ($\text{Na}_3\text{PO}_4 \cdot 12\text{H}_2\text{O}$) was purchased from Mallinckrodt.

Synthesis of $\text{Eu}-\text{CeO}_2$ nanowires

The $\text{Eu}-\text{CeO}_2$ nanowires were synthesized by a sol-gel reaction, followed by electrospinning to produce metal-polymer composite nanowires. The polymer template was subsequently removed through a two-step annealing process to produce the desired nanowire product. In a typical reaction, 0.25 g PVP was dissolved in 1.5 g dry MeOH while 0.3 g (0.70 mmol) $\text{Ce}(\text{NO}_3)_3$ and 0.0–0.06 g (0–0.13 mol) $\text{Eu}(\text{NO}_3)_3$ were dissolved in 1.0 g dry DMF. Once dissolved, the two solutions were rapidly stirred for 20 s until any visible precipitates dispersed, then gently shaken for 10 min to release any air bubbles. The solution was transferred to a syringe, which was connected to a long cannula terminated with a 25 mm, 16-gauge metal needle. The polymer solution was injected (*via* a syringe pump) at a speed of 0.8 mL h⁻¹ into an electric field with a voltage of 20 kV for a minimum of 15 min. A rotating drum covered with Al foil was placed 12 cm from the syringe tip and used as the counter electrode (Fig. S1†). To anneal, the metal-polymer nanowire films were removed from the collecting drum and sandwiched between two Si plates. The films were first gradually heated in ambient air (1 atm) to 220 °C over the course of 3 h ($\sim 1\text{ }^\circ\text{C min}^{-1}$) in an oven, held at that temperature for 16 h, then gradually cooled to room temperature over a 5 hour period. Once cooled, the Si plates containing the nanowire films were heated (air, 1 atm) to 950 °C over the course of 5 h ($\sim 3\text{ }^\circ\text{C min}^{-1}$) in a tube furnace, maintained at that temperature for 16 h, then cooled to room temperature over 6 h to yield white flakes weighing 5–20 mg.

Synthesis of $\text{Eu}-\text{CeO}_2$ nanorods

CeO_2 and $\text{Eu}-\text{CeO}_2$ nanorods were synthesized by modification of well-established hydrothermal procedures.^{53,54} In a typical reaction, 0.3 g (0.81 mmol) CeCl_3 and 0.0–0.04 g (0–0.12 mmol) EuCl_3 were dissolved in 4.5 mL H_2O , and 0.018 g (0.05 mmol) Na_3PO_4 dissolved in 13.9 mL of 2.5 M NaOH. The final reactant concentrations were 44 mM CeCl_3 , 0–6.5 mM EuCl_3 , and 2.7 mM Na_3PO_4 . The solutions were mixed and rapidly stirred in an ice bath at 0 °C for 20 min, transferred to a 50 mL Teflon screw-cap reactor, and heated at 100 °C in an oven for 16 h. The samples were washed while hot with three cycles of ethanol and water, dry at 100 °C, and ground to yield ~ 100 mg of a light yellow powder.

Synthesis of $\text{Eu}-\text{CeO}_2$ annealed nanorods

Annealed nanorods were produced from the $\text{Eu}-\text{CeO}_2$ nanorods as described above. The dry and ground nanorod powder was transferred to a quartz boat and placed in an oven. The annealed rods were heated to 500–800 °C (ambient air, 1 atm) over the course of an hour ($\sim 8\text{--}14\text{ }^\circ\text{C min}^{-1}$), maintained at that temperature for 16 h, then allowed to cool gradually to room temperature to yield a white/pale yellow powder.

Synthesis of $\text{Eu}-\text{CeO}_2$ nanocubes

CeO_2 and $\text{Eu}-\text{CeO}_2$ nanocubes were synthesized by a previously-reported hydrothermal procedure.^{53,54} Briefly, 0.4 g (0.92 mmol)



$\text{Ce}(\text{NO}_3)_3$ and 0.0–0.054 g $\text{Eu}(\text{NO}_3)_3$ (0–0.12 mmol) were dissolved in 6.6 mL H_2O . 13.3 mL of 15 M NaOH was added to yield final concentrations of 46 mM Ce^{3+} , 0.0–6.0 mM Eu^{3+} , and 10 M OH^- . The reaction mixture was rapidly stirred in an iced acetone bath at 0 °C for 20 min, transferred to a 20 mL stainless steel-coated Teflon vessel, and placed in an oven preheated to 180 °C for 16 h. After allowing the reactor to cool naturally, samples were washed with water, dry and ground into ~150 mg of white powder.

Characterization

The morphology of the Eu– CeO_2 nanorods was characterized by Transmission Electron Microscopy (TEM) and High Resolution TEM (HRTEM) using a JEOL 2100 TEM operating at 200 kV. Samples were first sonicated in de-ionized water for 2 min, then a drop of the suspension was transferred to a carbon coated copper grid and allowed to evaporate prior to analysis. Elemental data was collected using EDAX Energy Dispersive Spectroscopy Unit (EDS) attached to the JEOL 2100.

Powder X-ray diffraction (XRD) data was acquired using a Philips XRD3100 using $\text{Cu K}\alpha$ radiation, with step size of 0.02 deg and step time of 20 seconds in the 10–80° 2θ range. Sample peak positions were compared to CeO_2 reference sample data from the National Institute of Standards and Technology (NIST), Standard Reference Material 674b.⁵⁵

X-ray Photoelectron Spectroscopy (XPS) measurements were made on a PerkinElmer Phi 560 XPS/Auger system using a non-monochromatic Mg/Al X-ray source (nanorods, nanocubes, annealed nanorods) and a PHI 5000 Versa Probe II equipped with a monochromatic Al $\text{K}\alpha$ and a hemispherical analyzer (nanowires). All nanowire XPS data were taken with a pass energy of 23.5 eV, while XPS data for the other samples were taken with a pass energy of 100 eV for survey scans and 50 eV for detailed scans. The energy scale calibration for XPS is done using clean metal foils (polycrystalline Cu, Ag, Au) across the (binding) energy scale according to ASTM E2108-16. The scans were charge corrected (by a magnitude of no more than 1 eV) to adventitious carbon and assumed with have a binding energy of 284.6 eV. The Ce 3d and O 1s regions were fitted using CasaXPS software using Shirley backgrounds.

Spectroscopic analysis

For selected fluorescence measurements, the above Eu– CeO_2 nanomaterials were excited at a wavelength of 370 nm using a mercury lamp equipped with a ± 5 nm bandpass filter. Fluorescence images were taken on a Nikon fluorescence microscope and associated fluorescence spectra were recorded using an Ocean Optics 1000 series spectrometer interfaced to the above microscope. Fluorescence was acquired with a 100 ms integration time, unless otherwise noted.

Fluorescence and UV-Vis absorbance spectra were also recorded for these nanomaterials as aqueous suspensions. Three mg of 8 at% Eu– CeO_2 nanocubes were suspended in 5 mL of DI H_2O to make a stock solution. The stock solution was diluted until the peak absorbance was between 1.3 and 1.4. The diluted solutions were 112 $\mu\text{g mL}^{-1}$ for nanocubes, 260 $\mu\text{g mL}^{-1}$

for nanorods, 188 $\mu\text{g mL}^{-1}$ for annealed nanorods, and 75 $\mu\text{g mL}^{-1}$ for nanowires. These concentrations were used to obtain fluorescence and UV-Vis absorbance spectra of all suspended nanomaterials.

UV-Vis spectra were collected using an Agilent Cary 60 UV-Vis spectrometer in the 200–800 nm range. Selected fluorescence spectra were collected on a Shimadzu RF-5301 PC spectrofluorometer, with excitation at 375 nm, measuring emission from 400 nm to 700 nm, and using slit widths of 5 mm.

Results – nanomaterial characterization

Morphology

The morphologies of the four nanomaterials (nanowires, nanorods, nanocubes, annealed nanorods) were first characterized using transmission electron microscopy (TEM). The target Eu^{3+} concentration with regard to atomic percentage within each material ranges from 0% to 18% Eu^{3+} , as calculated by eqn (S1)[†] and based on experimental reactant concentrations.

Shown in Fig. 1 are the TEM images of the 8% Eu– CeO_2 of the above morphologies, where 8% indicates the target Eu concentration. This Eu^{3+} concentration is selected on the basis of its near-optimal emission intensity and associated absence of clustering/phase segregation of the lanthanide species in a given CeO_2 matrix. The nanowires are synthesized in and retain an interconnected network, due to the nature of the electrospinning process (Fig. 1a). The metal salts were dispersed into a polymer solution which was then injected into a strong electric field. Thin jets of this solution are ejected due to surface charge repulsion (Fig. S1[†]), whipping in transit to a collection drum, and depositing as long metal ion-loaded

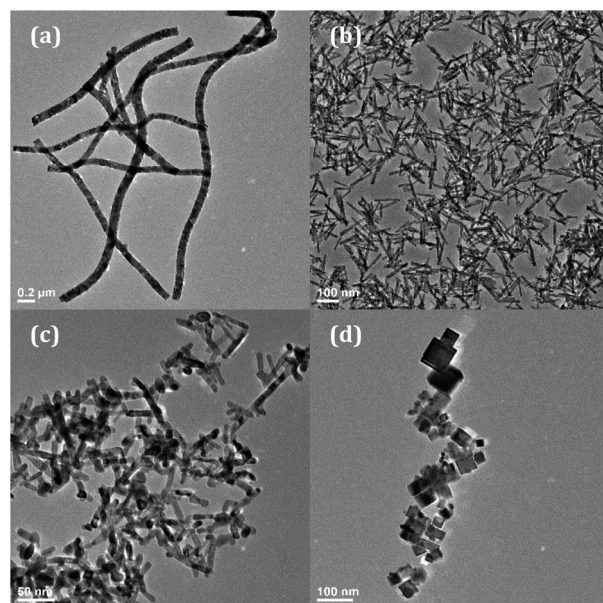


Fig. 1 TEM images of 8% Eu– CeO_2 (a) nanowires; (b) nanorods; (c) annealed nanorods; and (d) nanocubes.



polymer nanowires (Fig. S2†). Annealing removes the template without loss of the network morphology. The nanowire lengths are difficult to measure due to their non-linear morphology and a lack of discrete boundaries but are estimated to be \sim 1–2 μm . The nanowire diameter can be manipulated between 80 nm and 300 nm by adjusting the solvent ratio, but for this work the nanowire diameters are kept near 100 nm (Table 1 and Fig. S3†). Doping the nanowires with Eu^{3+} is accomplished by addition of $\text{Eu}(\text{NO}_3)_3$ to the electrospinning solution, and had no detectable influence on the resultant nanowire morphology.

In contrast to the nanowire template-based approach, the hydrothermal synthesis of nanocubes and nanorods uses the relative growth and oxidation of $\text{Ce}(\text{OH})_3$ and CeO_2 to control CeO_2 morphology. $\text{Ce}(\text{OH})_3$ precipitates upon mixing of the Ce^{3+} and OH^- solutions. By heating under pressure, $\text{Ce}(\text{OH})_3$ nanorods grow through Oswald ripening, which are converted to CeO_2 during the washing and drying steps. While occasional dense aggregates are observed, typically the nanorods grow with an average length of 91 nm and an average width of 11 nm (Fig. 1b and Table 1). The nanorods were annealed in air at 800 °C to remove defects and reduce the hydroxide presence. After annealing in air, some sintering was observed with increased fusion between rods (Fig. 1c). The nanorod length was reduced from 91 nm to 59 nm, and width increased from 11 nm to 19 nm (Table 1 and Fig. S3†).

By using higher concentrations of OH^- , eliminating Na_3PO_4 , and carrying out the hydrothermal reaction at 180 °C, nanocubes are synthesized instead of nanorods. The $\text{Ce}(\text{OH})_3$ nuclei dissolve given the higher pressure and temperature, and the Ce^{3+} is oxidized to Ce^{4+} prior to precipitation as small CeO_2 nuclei. The nanocubes grow through oriented attachment, with average edge lengths of about 25 nm (Fig. 1d, Table 1 and Fig. S3(f)†). Due to attraction between individual cubes, they appear as small clusters under 200 nm in diameter.

Crystallinity

The 8% Eu nanowires, nanocubes, nanorods, and annealed nanorods were characterized through powder X-ray diffraction (XRD) to determine their crystal structure, detect any possible phase separation of europium oxide (Eu_2O_3) or Ce_2O_3 , and estimate crystalline domain size. CeO_2 crystallizes in a cubic fluorite structure, with cerium ions arranged in a face centered cubic lattice and oxygen ions in the tetrahedral holes. The XRD patterns of 8% Eu– CeO_2 nanorods, nanocubes, nanowires, and annealed nanorods are shown in Fig. S4,† indicating that all four morphologies are composed of CeO_2 in the cubic fluorite phase.¹² No evidence of Eu_2O_3 or other crystal phases is

Table 1 Dimensions of 8% Eu– CeO_2 nanomaterials as determined by TEM image analysis

Sample	Width (nm)	Length (nm)
Nanowires	108 \pm 25	$>1\ \mu\text{m}$
Nanorods	11 \pm 3	91 \pm 21
Annealed nanorods	19 \pm 6	59 \pm 29
Nanocubes	25 \pm 11	—

observed in any sample. Relative crystalline domain sizes were determined by a Scherrer analysis of broadening from the (111) reflection (ESI†). The calculated domain sizes are consistent with the peak broadening seen in Fig. S4,† with the nanorods and nanocubes assigned the smallest and largest domains, respectively (Table 2). Annealing the nanorods increases the domain size from 6 nm to 16 nm, consistent with sintering and fusion of the nanorods.

Each morphology was also characterized using HRTEM to further investigate differences in crystallinity and exposed lattice faces. All lattice spacings observed in each sample morphology are assignable to the (111), (200), and (220) planes of the cubic fluorite CeO_2 crystal structure.¹² However, the samples differed regarding which of the three CeO_2 planes were exposed, the size of the crystalline domains, and whether the nanomaterial was monocrystalline or polycrystalline.

At high magnification, the 8% Eu– CeO_2 nanowires are composed of fused nanoparticles about 15–20 nm in diameter (Fig. 2a). The lattice spacing is difficult to image, due to reduced electron transmission through the thick nanowires. Despite this, some fringes can be observed in small protruding nanoparticles. Each of these nanoparticles is monocrystalline, typically with the CeO_2 cubic fluorite (111) plane exposed. Occasionally one crystalline domain expands past one nanoparticle into the neighboring fused particles. The 8% Eu– CeO_2 nanocubes are also monocrystalline, with clusters of nanocubes commonly consisting of one domain due to their growth through oriented attachment (Fig. 2d). Consistent with previously published literature, the nanocubes expose higher energy (200) lattice planes, with the (111) and (220) lattice fringes occasionally observed.⁵⁶

In contrast, the nanorods are polycrystalline, with each rod exposing several crystalline planes within one rod (Fig. 2b). The highest energy plane, (220), often runs perpendicular to the length of the rod or needle, while (111) planes run both diagonally and parallel to the nanorod length. Two to five nanometer domains are also often observed, with random orientation relative to the remainder of the particle. The conversion from $\text{Ce}(\text{OH})_3$ to CeO_2 during washing and drying results in rapid crystallization at several locations within a single particle, consistent with the observed polycrystallinity. Upon annealing the nanorods, the individual crystalline domains are sintered into one large domain that encompasses the entire nanorod (Fig. 2c). The (220) plane is no longer observed, with only the (111) lattice fringes observed, similar to the nanowires.

Table 2 Full-width half-maximum of (111) peaks from ~8% Eu– CeO_2 nanomaterials, with associated crystalline domain sizes as determined by the Scherrer equation

Sample	FWHM (2 Θ)	XRD crystalline domain (nm)
Nanowires	0.5	17
Nanocubes	0.38	22
Nanorods	1.44	6
Annealed nanorods	0.58	16



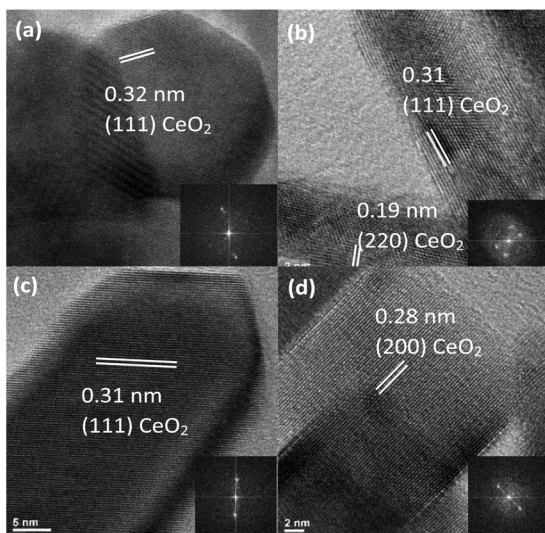


Fig. 2 HR-TEM images with lattice spacings of 8% Eu–CeO₂ (a) nanowires, (b) nanorods, (c) annealed nanorods, and (d) nanocubes. Inset in each HRTEM image is the respective fast fourier transform (FFT).

Elemental characterization

All four morphologies were characterized using energy dispersive X-ray spectroscopy (EDS) to determine elemental composition. The EDS spectra showed the expected elements, namely

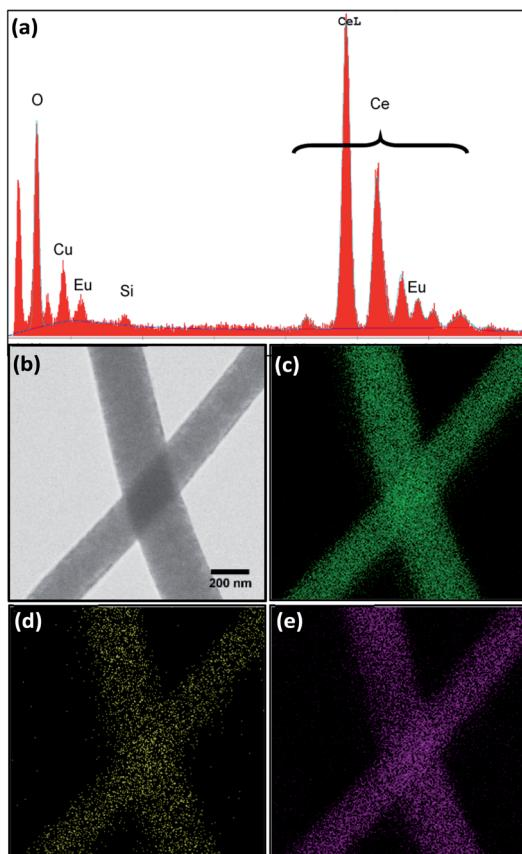


Fig. 3 (a) Representative EDS spectrum of 8% Eu–CeO₂ nanowires, with corresponding (b) STEM image, and elemental maps of (c) cerium (d) europium, and (e) oxygen, elemental maps.

cerium, oxygen, and europium (Fig. 3a). Copper and carbon peaks were also observed due to the carbon-coated copper mesh sample holder and a Si artefact was occasionally observed, with no other contaminants. Oxygen, europium, and cerium were relatively evenly distributed throughout the nanowires, as seen by elemental mapping of the 8% Eu–CeO₂ nanowires (Fig. 3b–e). The atomic concentrations were calculated assuming cerium, europium, and oxygen to be the only significant components (Tables 3, S1 and S2†).

The use of EDS to quantify oxygen concentrations is somewhat unreliable as oxygen is a relatively mobile species in a focused electron beam. The nanorod and annealed nanorod morphologies show slightly elevated oxygen concentrations relative to the nanocube and nanowire samples. Since the nanorods are initially synthesized as Ce(OH)₃ with rapid oxidation to CeO₂, trace amounts of Ce(OH)₃ may remain in the nanorod, increasing the oxygen-to-cerium ratio. The oxygen concentration is somewhat lower in the nanowires and nanocubes compared to the rod samples. The nanocube synthesis is driven by oriented attachment of CeO₂ nanoparticles, reducing the likelihood of trapped hydroxide species, while the nanowires have a slightly higher concentration of Eu³⁺, increasing the oxygen defect concentration.

XPS analysis

To more quantitatively determine the influence of morphology on the Ce³⁺/Ce⁴⁺ ratio and oxygen defect concentration, XPS measurements were performed on the four 8% Eu–CeO₂ nanomaterials (nanorods, nanocubes, nanowires, annealed nanorods), as well as undoped CeO₂ nanorods. After fitting of the Eu–CeO₂ nanorod's core level Ce 3d spectral region, six peaks at 881.8, 888.2, 898.0, 900.6, 906.7, and 916.4 eV were assigned to Ce⁴⁺, while two peaks at 884.7 and 903.2 eV were assigned to Ce³⁺ (Fig. 4a and Table S4†). Similar components were identified in the Ce 3d spectrum of the Eu–CeO₂ annealed rods, with negligible shifts in binding energy of 0.3 eV or less (Fig. 4b and Table S4†). Similar peak fitting was used for the Eu–CeO₂ nanowires and Eu–CeO₂ nanocubes (Tables S3, S4 and Fig. S5†).

The concentration of Ce³⁺ ions within the nanomaterial can then be calculated using the integrated areas of the fitted peaks, as written in eqn (1) where A_x is the area of the peak “x”.

$$[\text{Ce}^{3+}] = \frac{A_{u'} + A_{v'}}{A_u + A_{u''} + A_{u'''} + A_v + A_{v''} + A_{v'''}} \quad (1)$$

Since the nanorods are synthesized as Ce(OH)₃ prior to drying with no high temperature annealing treatment, the Ce³⁺ concentration was highest in the nanorod morphology (20.1%), followed by the nanocubes (15.1%), annealed nanorods (10.4%), and finally the nanowires (8.2%).

The O 1s spectrum for the above CeO₂ nanomaterials (Fig. 4c and d) was fitted to show two peaks, O_α and O_β. O_α is typically associated with lattice oxygen and O_β accounts for surface oxygen as well as oxygen near crystal defects. The undoped CeO₂ nanorods had a O_β percentage of 17.4%, which increased upon doping to 25.7% due to the internal defects induced by the

Table 3 Atomic concentrations of oxygen, cerium, and europium within 8% Eu–CeO₂ nanomaterials, as determined by EDS. Cerium and europium concentrations are also included in the absence of oxygen to provide the metals only atomic percentage

Sample	Metal and oxygen concentrations			Metal elements only	
	At% O	At% Ce	At% Eu	At% Ce	At% Eu
Nanowire	53.1 ± 4.3	42.3 ± 3.8	4.6 ± 0.9	90.3 ± 1.7	9.7 ± 1.7
Nanorod	62.1 ± 5.5	34.2 ± 4.6	3.7 ± 0.9	92.1 ± 1.7	7.9 ± 1.7
Annealed nanorod	60.2 ± 1.9	36.9 ± 2.1	2.8 ± 0.4	93.0 ± 0.9	7.0 ± 0.9
Nanocube	54.3 ± 3.6	42.6 ± 3.7	3.1 ± 0.2	93.2 ± 0.9	6.8 ± 0.9

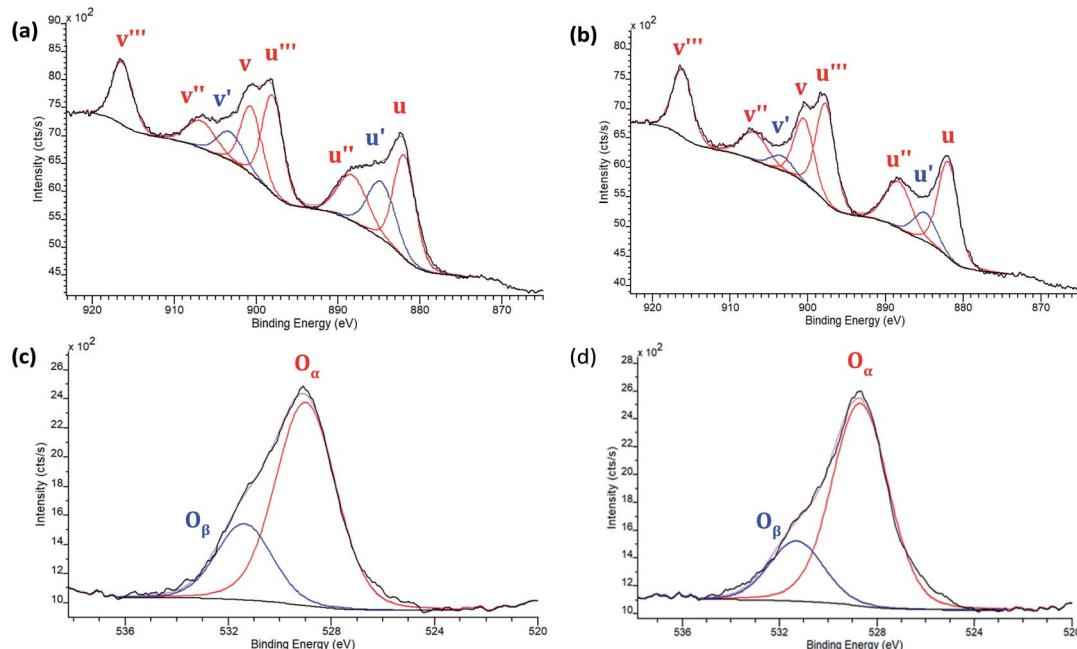


Fig. 4 XPS spectra of 8% Eu–CeO₂ (a) Ce 3d region of nanorods; (b) Ce 3d annealed nanorods; and (c) O 1s region of nanorods, and (d) O 1s of annealed nanorods.

presence of Eu³⁺. Annealing the nanorods reduces the percentage of O_B down to 20.2%, as defects and/or surface hydroxides are eliminated. The nanocubes and nanowires had the lowest O_B concentrations of 9.7% and 13.6% respectively.

Results – optical properties

Europium(III) is well known for its hypersensitive electric dipole (ED) transition, $^5D_0 \rightarrow ^7F_2$, which is parity forbidden, and thus is particularly sensitive to surrounding inversion symmetry. The emission is forbidden if the ion is located in more symmetrical environments, and therefore Eu³⁺ has been used as to probe local structure.⁵⁷ In addition to this ED hypersensitive $^5D_0 \rightarrow ^7F_2$ transition emitting in the 610–630 nm region, europium has another transition of particular interest, the magnetic dipole (MD) $^5D_0 \rightarrow ^7F_1$ transition emitting near 590 nm which is relatively insensitive to the local environment.⁵⁸

Analysis of asymmetry about the Eu³⁺ ion is well-established, typically quantified by the asymmetry ratio, R_{21} , which compares the integrated area of the two transitions as defined in eqn (2).⁵⁸ Higher R_{21} values correspond with insertion of the Eu³⁺ ion into

relatively more asymmetric environments, due to the increased emission intensity of the hypersensitive transition.

$$R_{21} = \frac{I_{^5D_0 \rightarrow ^7F_2}}{I_{^5D_0 \rightarrow ^7F_1}} \quad (2)$$

Fluorescence from europium-doped cerium oxide has been previously reported in several CeO₂ morphologies, including particles,³³ wires,⁵¹ and rods.⁵⁰ The Eu³⁺ ions substitute into the highly symmetrical Ce⁴⁺ site, suppressing emission through the $^5D_0 \rightarrow ^7F_2$ transition, and lowering the R_{21} ratio.^{47,59} Introduction of defects, such as oxygen vacancies and accompanying Ce³⁺ ions also disrupts the CeO₂ lattice, breaking the inversion symmetry and increasing the asymmetry ratio.⁶⁰ However, these defects may also facilitate non-radiative relaxation, thereby suppressing Eu³⁺ emission intensity.

Fluorescence: excitation at 370 nm

The nanomaterials were first investigated as dry powders or films using a 370 nm excitation wavelength to minimize scattering (as seen in the UV-Vis absorption spectra). Upon



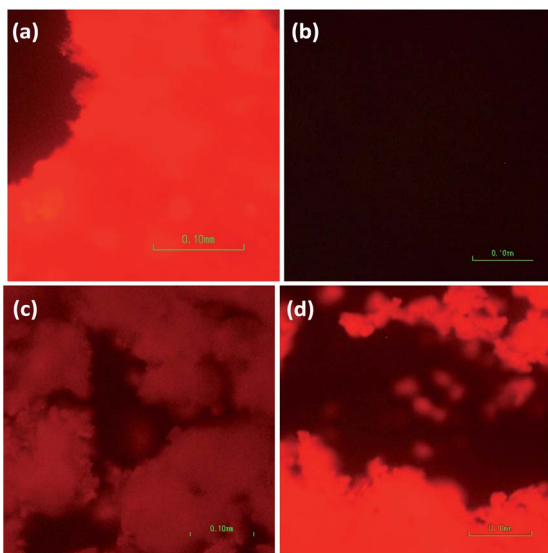


Fig. 5 Images of emission from 8 at% Eu–CeO₂ (a) nanowires, (b) nanorods, (c) annealed nanorods, and (d) nanocubes, following excitation at 375 nm, with acquisition time of 800 ms.

excitation at 370 nm, the 8% Eu–CeO₂ nanocubes, nanowires, and annealed nanorods all exhibit strong red fluorescence (Fig. 5a, c, d and 6), associated with previously reported Eu³⁺ luminescence spectra of Eu–CeO₂ materials.^{33,50,51} In contrast, no visibly detectable emission was observed from the as prepared nanorods (Fig. 5b).

Eu–CeO₂ systems are prone to Eu³⁺ fluorescence quenching through non-radiative relaxation facilitated by surface hydroxyls or oxygen vacancies within the material,^{28,33} so the 8% Eu–CeO₂ nanorods were annealed to increase Eu³⁺ emission intensity by ideally removing defects. Weak emission is first detected after annealing to 400 °C and intensifies with increasing annealing temperature (Fig. 7). The asymmetry ratio decreases with increasing annealing temperature, driven in part by the sharpening of the hypersensitive peak at 610 nm due to reduction of a shoulder near 606 nm. The presence of this shoulder at low annealing temperatures suggests that the symmetry around the europium ions may be broken by several different types of defects (Ce³⁺, oxygen vacancy, hydroxyl group, *etc.*).⁶¹ The removal of some of these defects, leaving only Ce³⁺ and oxygen

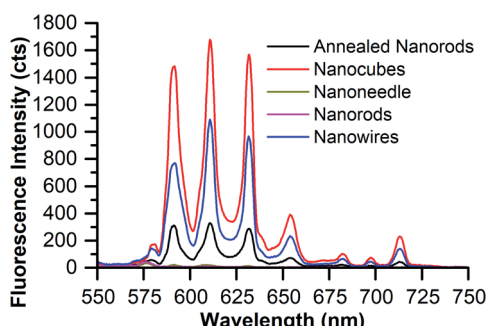


Fig. 6 Emission of 8% Eu–CeO₂ dry powder or film samples following excitation at 375 nm with 100 ms acquisition time.

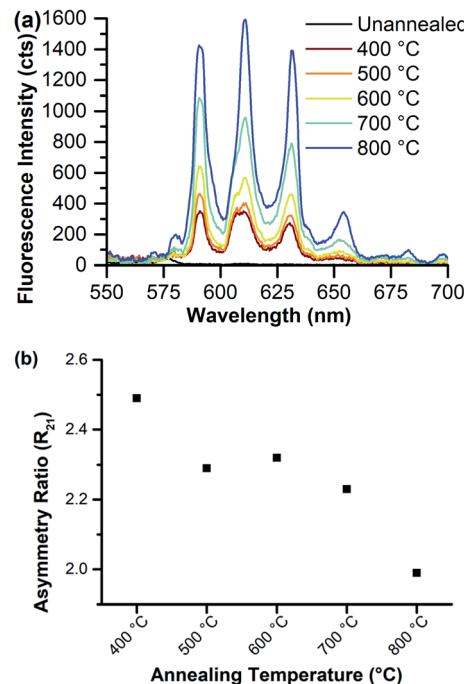


Fig. 7 8% Eu–CeO₂ nanorods annealed to various temperatures and excited at 375 nm, showing (a) fluorescence spectra; and (b) asymmetry ratio values as a function of annealing temperature.

vacancies as required by europium-induced charge balance, is reflected in the peak sharpening and disappearance of the shoulder if the nanorods are annealed to 700 °C or higher.

It should be pointed out, however, that the strongly fluorescing nanocubes are also synthesized through a hydrothermal reaction and should also be covered with the same functional moieties. The difference in emission of the nanorods and nanocubes may be explained in part by the rapid oxidation of the nanorods and their smaller crystal domains. These domains in principle allow more defects, which may act as sites of emission quenching. Hydroxide species not removed from the nanorods due to rapid oxidation also act to quench the Eu³⁺ emission.

Therefore, we propose two separate stages of fluorescence activation. Quenching species such as surface hydroxyls are eliminated at temperatures below 600 °C (Fig. S6†) so the nanorods exhibit weak Eu³⁺ emission. Removal of internal and/or surface defects such as oxygen vacancies and Ce³⁺ defects occurs at higher temperatures. The removal of these defects reduces the asymmetry about the Eu³⁺ centers, as reflected in the reduction of the asymmetry ratio with a concurrent enhancement of fluorescence intensity.

Fluorescence: excitation at 340 nm

The emission from suspended Eu–CeO₂ nanomaterials was then measured following excitation at 340 nm, the absorbance maximum (Fig. S7 and S8†). Comparisons of emission intensity between morphologies is not feasible, as each morphology is suspended using a different concentration limited by size-dependent scattering. However, the Eu³⁺ asymmetry ratios may still be calculated and compared as they are an intrinsic



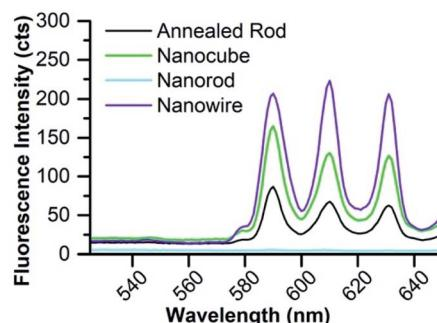


Fig. 8 Emission of 8 at% Eu–CeO₂ nanowires (75 µg mL^{−1}), nanorods (260 µg mL^{−1}), nanocubes (112 µg mL^{−1}), nanorods (260 µg mL^{−1}) and annealed nanorods (188 µg mL^{−1}) following excitation at 340 nm with 100 ms acquisition.

property and independent of concentration. Furthermore, the influence of Eu³⁺ concentration may be compared between samples of similar morphology, due to the negligible influence of Eu³⁺ on morphology and size.

As previously described, the nanocubes have the most intense emission of the four morphologies when excited as a dry powder at 375 nm. For this reason, the excitation spectrum was collected for the nanocubes, monitoring emission at 590 nm (Fig. S9†). As anticipated, the maximum emission is observed with excitation near 340 nm, consistent with CT excitation of host CeO₂ and energy transfer to Eu³⁺. Insignificant peaks are also observed at 500 nm and 620 nm, representing weak direct excitation of Eu³⁺ through the ⁷F₀ → ⁵D₀ and ⁷F₂ → ⁵D₀.

Representative fluorescence spectra of the suspended 8% Eu–CeO₂ samples, following excitation at 340 nm using a commercial fluorimeter are shown in Fig. 8. The asymmetry ratios (R_{21}) calculated from these spectra are listed in Table 4. The asymmetry ratio loosely tracks with the crystalline domain size, with the nanocubes showing the lowest asymmetry followed by the annealed nanorods and finally the nanowires. As CeO₂ nanoparticles with small crystalline domains typically exhibit higher defect concentrations,⁶² Eu³⁺ ions doped into materials with small domains are more likely to be in an asymmetrical site. However, compared to the variation in asymmetry ratio observed with changing Eu³⁺ concentration, the differences between morphologies are relatively small.

Each morphology was synthesized at target Eu³⁺ concentrations of 0–15%, then analyzed for differences in Eu³⁺ emission

Table 4 Asymmetry ratio (R_{21}) following excitation at 340 nm of 8 at% Eu–CeO₂ nanomaterials at concentrations detailed in Fig. 9. Columns labelled ⁵D₀ → ⁷F₁ and ⁵D₀ → ⁷F₂ refer to relative emission intensities for the respective transitions for a given sample

Sample	$I_{5D_0 \rightarrow 7F_1}$	$I_{5D_0 \rightarrow 7F_2}$	Asymmetry ratio (R_{21})
Nanowire	2087	4030	1.93
Nanorod	145	72	1.99
Annealed nanorod	1420	782	1.81
Nanocube	2636	1512	1.74

intensity and asymmetry ratio (Table 4 and Fig. 9). Emission from the nanorods was extremely weak, regardless of europium concentration or emission acquisition parameters. In addition, no emission is observed for any undoped morphology except the nanowires with an extremely weak ⁷F₀ → ⁵D₁ emission at 590 nm, attributed to a small Eu³⁺ contamination. Therefore,

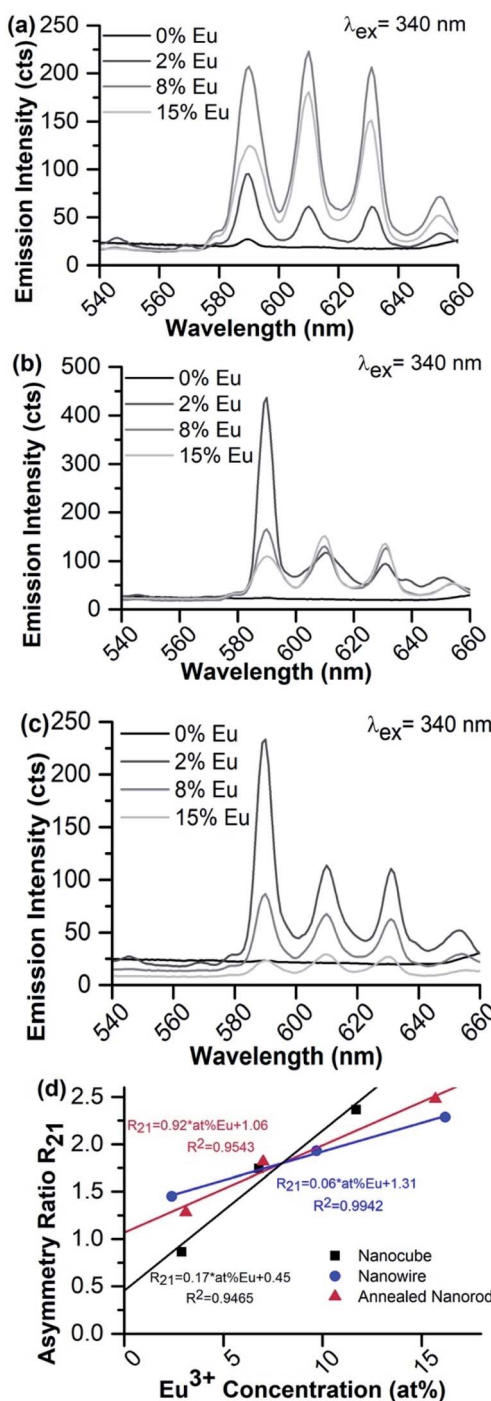


Fig. 9 Fluorescence of target 0–15% Eu³⁺-doped CeO₂ (a) nanowires; (b) nanocubes; (c) annealed nanorods; and (d) the calculated asymmetry ratio for various Eu³⁺ concentrations, all following excitation at 340 nm.



the following analysis is limited to the doped nanowires, nanocubes, and annealed nanorods.

If CeO_2 is doped with relatively low concentrations of europium, the europium substitutes into the highly symmetrical Ce^{4+} sites of the CeO_2 crystal lattice with minimal nearby asymmetry, so emission from the hypersensitive $^7\text{F}_0 \rightarrow ^5\text{D}_2$ transition at 610 nm and 630 nm is suppressed.³⁴ Increasing the Eu^{3+} concentration generates more Ce^{3+} defects and oxygen vacancies, breaking the inversion symmetry about the emitting ion and allowing the hypersensitive transition. However, most Eu^{3+} -containing nanomaterials suffer from concentration quenching, limiting emission intensity overall at higher doping concentrations.

The fluorescence spectra of the 2% $\text{Eu}-\text{CeO}_2$ nanomaterials are all dominated by intense emission from the $^7\text{F}_0 \rightarrow ^5\text{D}_1$ MD transition at 590 nm, while emission through the $^7\text{F}_0 \rightarrow ^5\text{D}_2$ hypersensitive peaks at 610 and 630 nm is relatively suppressed (Fig. 9). Increasing the Eu^{3+} concentration to 8% quenches the MD transition by about 60% for the nanocubes and annealed nanorods, while the intensity doubles for the nanowires. This emission is further quenched in the most heavily-doped nanocubes and annealed nanorods, with an overall decrease in fluorescence of 60% and 85%, respectively. The MD transition is also less intense in the 15% Eu^{3+} nanowire samples compared to the 8% sample, but is still relatively 60% stronger than the 2% doped sample.

Manipulation of the Eu^{3+} concentration has a unique impact on the hypersensitive emission intensity from each of the three morphologies. In the nanocubes, the fluorescence intensity increases by less than 10%, consistent with the introduction of new defects into the crystal lattice. In contrast, the hypersensitive transition emission steadily weakens with increasing Eu^{3+} concentrations in the annealed nanorods, suggesting an increased likelihood of lanthanide self-quenching. In the nanowires, the hypersensitive transition mirrors the behavior of the MD transition, more than doubling in intensity when the Eu^{3+} concentration is increased from 2 at% to 8 at%, then slightly weakening at 8 at% to 15 at% respectively. The calculated asymmetry ratio reflects these trends between materials (Fig. 9d). The R_{21} ratio is more sensitive to the Eu^{3+} concentration in the nanocube morphology compared to the nanowires or annealed nanorods, due to the significant quenching at 590 nm in the nanocube sample coupled with slight intensification of the hypersensitive transition. R_{21} also increases for the nanowires and annealed nanorods, but in a manner far less sensitive to $[\text{Eu}^{3+}]$ compared to the nanocubes. Annealing the CeO_2 , as required during synthesis of the nanowires and annealed nanorods (Table S5†), minimizes the presence of defects such as oxygen vacancies or Ce^{3+} ions, reducing the asymmetry observed by the emitting Eu^{3+} .

Conclusions

A series of doped CeO_2 nanomaterials have been synthesized with morphological control, and subsequently doped with europium in an effort to understand the relationship between morphology and fluorescent properties. The four morphologies present a range of dimensions, $\text{Ce}^{3+}/\text{Ce}^{4+}$ ratios, surface chemistries, and crystalline defects with an important impact on the Eu^{3+} emission. The CeO_2 nanowires and nanocubes were

successful hosts for Eu^{3+} doping, both intensely emitting when excited at 340 nm due to large crystalline domains and minimal defects which would otherwise quench the fluorescence. The CeO_2 nanorods were non-emissive as synthesized, requiring an annealing treatment to remove surface hydroxyls and internal defects to avoid quenching of the emission from Eu^{3+} .

While all three emissive morphologies exhibit the expected increase in asymmetry ratio with doping concentration, the sensitivity of the Eu^{3+} hypersensitive transition, as determined through the asymmetry ratio, to the Eu^{3+} concentration was highly morphologically dependent. The nanocube morphology was particularly sensitive to increases in the doping concentration, with minimal change in the hypersensitive transition despite strong lanthanide self-quenching as indicated by the suppression of the magnetic dipole transition. Also, on a pragmatic level, the nanocubes are much smaller than the nanowires, with edge lengths of ~ 25 (± 10 nm) *versus* nanowires, which are ~ 100 nm thick and microns long. Due to their small size, the nanocubes disperse in water with significantly reduced scattering compared to the nanowire samples. Thus, optimal photophysical outcome, for a discrete, strongly emissive platform, lies with this cubic nanostructure shape. Further investigations of the utility of selected doped cerium oxide nanostructures such as these in applications such as cell labeling, are underway.

Conflicts of interest

There are no conflicts to declare.

Acknowledgements

The authors gratefully thank Dr Jiechao Jiang at the University of Texas-Arlington and Mr Christopher Cormier at the University of Texas-Dallas for assistance with XPS measurements of selected samples. AED and JLC gratefully acknowledge financial support of this research by the Robert A. Welch Foundation (Grant P-1212). RMW acknowledges the support of the Erik Jonsson Distinguished Chair.

Notes and references

- 1 J. Kašpar, P. Fornasiero and M. Graziani, *Catal. Today*, 1999, **50**, 285–298.
- 2 V. V. Kharton, F. M. Figueiredo, L. Navarro, E. N. Naumovich, A. V. Kovalevsky, A. A. Yaremchenko, A. P. Viskup, A. Carneiro, F. M. B. Marques and J. R. Frade, *J. Mater. Sci.*, 2001, **36**, 1105–1117.
- 3 B. C. Steele, *Solid State Ionics*, 2000, **129**, 95–110.
- 4 R. W. Tarnuzzer, J. Colon, S. Patil and S. Seal, *Nano Lett.*, 2005, **5**, 2573–2577.
- 5 N. Izu, W. Shin, N. Murayama and S. Kanzaki, *Sens. Actuators, B*, 2002, **87**, 95–98.
- 6 B. Liu, Z. Sun, P.-J. J. Huang and J. Liu, *J. Am. Chem. Soc.*, 2015, **137**, 1290–1295.
- 7 T. Pirmohamed, J. M. Dowding, S. Singh, B. Wasserman, E. Heckert, A. S. Karakoti, J. E. King, S. Seal and W. T. Self, *Chem. Commun.*, 2010, **46**, 2736–2738.



8 C. Korsvik, S. Patil, S. Seal and W. Self, *Chem. Commun.*, 2007, **10**, 1056–1058.

9 H.-I. Chen and H.-Y. Chang, *Ceram. Int.*, 2005, **31**, 795–802.

10 M. Yamashita, K. Kameyama, S. Yabe, S. Yoshida, Y. Fujishiro, T. Kawai and T. Sato, *J. Mater. Sci.*, 2002, **37**, 683–687.

11 Z. Ji, X. Wang, H. Zhang, S. Lin, H. Meng, B. Sun, S. George, T. Xia, A. E. Nel and J. I. Zink, *ACS Nano*, 2012, **6**, 5366–5380.

12 H.-X. Mai, L.-D. Sun, Y.-W. Zhang, R. Si, W. Feng, H.-P. Zhang, H.-C. Liu and C.-H. Yan, *J. Phys. Chem. B*, 2005, **109**, 24380–24385.

13 Z. L. Wang and X. Feng, *J. Phys. Chem. B*, 2003, **107**, 13563–13566.

14 C. Laberty-Robert, J. W. Long, E. M. Lucas, K. A. Pettigrew, R. M. Stroud, M. S. Doescher and D. R. Rolison, *Chem. Mater.*, 2006, **18**, 50–58.

15 N. Özer, *Sol. Energy Mater. Sol. Cells*, 2001, **68**, 391–400.

16 A. Vantomme, Z.-Y. Yuan, G. Du and B.-L. Su, *Langmuir*, 2005, **21**, 1132–1135.

17 X.-h. Lu, X. Huang, S.-l. Xie, D.-z. Zheng, Z.-q. Liu, C.-l. Liang and Y.-X. Tong, *Langmuir*, 2010, **26**, 7569–7573.

18 S. Yang and L. Gao, *J. Am. Chem. Soc.*, 2006, **128**, 9330–9331.

19 X. Q. Fu, C. Wang, H. C. Yu, Y. G. Wang and T. H. Wang, *Nanotechnology*, 2007, **18**, 145503.

20 K. Zhou, Z. Yang and S. Yang, *Chem. Mater.*, 2007, **19**, 1215–1217.

21 F. Esch, S. Fabris, L. Zhou, T. Montini, C. Africh, P. Fornasiero, G. Comelli and R. Rosei, *Science*, 2005, **309**, 752.

22 E. G. Heckert, A. S. Karakoti, S. Seal and W. T. Self, *Biomaterials*, 2008, **29**, 2705–2709.

23 Y. Hernández-Castillo, M. García-Hernández, A. López-Marure, J. H. Luna-Domínguez, P. Y. López-Camacho and Á. d. J. Morales-Ramírez, *Ceram. Int.*, 2019, **45**, 2303–2308.

24 I. Celardo, J. Z. Pedersen, E. Traversa and L. Ghibelli, *Nanoscale*, 2011, **3**, 1411–1420.

25 C. Sun, H. Li and L. Chen, *Energy Environ. Sci.*, 2012, **5**, 8475.

26 S. Deshpande, S. Patil, S. V. N. T. Kuchibhatla and S. Seal, *Appl. Phys. Lett.*, 2005, **87**, 133113.

27 M. Nolan, *J. Phys. Chem. C*, 2011, **115**, 6671–6681.

28 B. Suresh, T. Ranjith, I. Talgat, D. Richard, E. M. Artém, S. Alfons and S. Sudipta, *Nanotechnology*, 2009, **20**, 085713.

29 V. Stetsovych, Doctor of Philosophy Doctoral Thesis, Charles University, 2015.

30 W. Huang, P. Shuk and M. Greenblatt, *Chem. Mater.*, 1997, **9**, 2240–2245.

31 D. Zhang, X. Du, L. Shi and R. Gao, *Dalton Trans.*, 2012, **41**, 14455–14475.

32 D. Avram, M. Sanchez-Dominguez, B. Cojocaru, M. Florea, V. Parvulescu and C. Tiseanu, *J. Phys. Chem. C*, 2015, **119**, 16303–16313.

33 A. Kumar, S. Babu, A. S. Karakoti, A. Schulte and S. Seal, *Langmuir*, 2009, **25**, 10998–11007.

34 X. Liu, S. Chen and X. Wang, *J. Lumin.*, 2007, **127**, 650–654.

35 J. Wu, S. Shi, X. Wang, J. Li, R. Zong and W. Chen, *J. Mater. Chem. C*, 2014, **2**, 2786–2792.

36 H. Guo, *J. Solid State Chem.*, 2007, **180**, 127–131.

37 J.-H. Cho, M. Bass, S. Babu, J. M. Dowding, W. T. Self and S. Seal, *J. Lumin.*, 2012, **132**, 743–749.

38 L. Li, H. K. Yang, B. K. Moon, Z. Fu, C. Guo, J. H. Jeong, S. S. Yi, K. Jang and H. S. Lee, *J. Phys. Chem. C*, 2009, **113**, 610–617.

39 B. Chen, L. Wang, Y. Xiao, F. R. Fronczeck, M. Xue, Y. Cui and G. Qian, *Angew. Chem., Int. Ed.*, 2009, **48**, 500–503.

40 C. P. Montgomery, B. S. Murray, E. J. New, R. Pal and D. Parker, *Acc. Chem. Res.*, 2009, **42**, 925–937.

41 P. P. Ortega, L. S. R. Rocha, J. A. Cortés, M. A. Ramirez, C. Buono, M. A. Ponce and A. Z. Simões, *Appl. Surf. Sci.*, 2019, **464**, 692–699.

42 A. Othman, A. Hayat and S. Andreeescu, *ACS Appl. Nano Mater.*, 2018, **1**, 5722–5735.

43 E. O. Gubernatorova, X. Liu, A. Othman, W. T. Muraoka, E. P. Koroleva, S. Andreeescu and A. V. Tumanov, *Adv. Healthcare Mater.*, 2017, **6**, 1700176.

44 D. Avram, C. Rotaru, B. Cojocaru, M. Sanchez-Dominguez, M. Florea and C. Tiseanu, *J. Mater. Sci.*, 2014, **49**, 2117–2126.

45 V. I. Parvulescu and C. Tiseanu, *Catal. Today*, 2015, **253**, 33–39.

46 S. Babu, A. Schulte and S. Seal, *Appl. Phys. Lett.*, 2008, **92**, 123112.

47 G. Vimal, K. P. Mani, P. R. Biju, C. Joseph, N. V. Unnikrishnan and M. A. Ittyachen, *Appl. Nanosci.*, 2015, **5**, 837–846.

48 J. Lee, Y. Park, S. Woo Joo and Y. Sohn, *Doping-Concentration and Annealing Effects on Photoluminescence Profile of Eu(III)-doped CeO₂ nanorods*, 2014.

49 A. V. Thorat, T. Ghoshal, P. Carolan, J. D. Holmes and M. A. Morris, *J. Phys. Chem. C*, 2014, **118**, 10700–10710.

50 W. Gao, J. Li, X. Zhou, Z. Zhang, Y. Ma and Y. Qu, *J. Mater. Chem. C*, 2014, **2**, 8729–8735.

51 D. Fang, M. Zhang, Z. Luo, T. Cao, Q. Wang, Z. Zhou, M. Jiang and C. Xiong, *Opt. Mater.*, 2014, **38**, 1–5.

52 C. Tiseanu, V. Parvulescu, D. Avram, B. Cojocaru, M. Boutonnet and M. Sanchez-Dominguez, *Phys. Chem. Chem. Phys.*, 2014, **16**, 703–710.

53 H. Mai, L. Sun, Y. Zhang, R. Si, W. Feng, H. Zhang, H. Liu and C. Yan, *J. Phys. Chem. B*, 2005, **109**, 24380–24385.

54 Q. Wu, F. Zhang, P. Xiao, H. Tao, X. Wang, Z. Hu and Y. Lü, *J. Phys. Chem. C*, 2008, **112**, 17076–17080.

55 SRM 674b, *X-Ray Powder Diffraction Intensity Set for Quantitative Analysis by X-Ray Powder Diffraction*, National Institute of Standards and Technology, U.S. Department of Commerce, Gaithersburg, MD, 2017.

56 T. Sakthivel, S. Das, A. Kumar, D. L. Reid, A. Gupta, D. C. Sayle and S. Seal, *ChemPlusChem*, 2013, **78**, 1446–1455.

57 B. R. Judd, *J. Chem. Phys.*, 1966, **44**, 839–840.

58 K. Binnemans, *Coord. Chem. Rev.*, 2015, **295**, 1–45.

59 A. Sharma, M. Varshney, J. Park, T. K. Ha, K. H. Chae and H. J. Shin, *Phys. Chem. Chem. Phys.*, 2015, **17**, 30065–30075.

60 I. E. Kolesnikov, A. V. Povolotskiy, D. V. Mamonova, E. Y. Kolesnikov, A. V. Kurochkin, E. Lähderanta and M. D. Mikhailov, *J. Rare Earths*, 2018, **36**, 474–481.

61 T. Aubert, F. Grasset, M. Potel, V. Nazabal, T. Cardinal, S. Pechev, N. Saito, N. Ohashi and H. Haneda, *Sci. Technol. Adv. Mater.*, 2010, **11**, 044401.

62 X. D. Zhou and W. Huebner, *Appl. Phys. Lett.*, 2001, **79**, 3512–3514.

